

Observation of a dynamic magneto-chiral instability in photoexcited tellurium

Yijing Huang,^{1,2,*} Nick Abboud,^{3,*} Yinchuan Lv,^{1,2} Penghao Zhu,^{1,4,5} Azel Murzabekova,^{1,2} Changjun Lee,^{6,2} Emma A. Pappas,^{1,2} Dominic Petruzzi,^{1,2} Jason Y. Yan,^{1,2} Dipanjan Chauduri,^{1,2} Peter Abbamonte,^{1,2} Daniel P. Shoemaker,^{6,2} Rafael M. Fernandes,^{1,4} Jorge Noronha,³ and Fahad Mahmood^{1,2}

¹*Department of Physics, The Grainger College of Engineering,
University of Illinois Urbana-Champaign, Urbana, Illinois 61801, USA*

²*Materials Research Laboratory, The Grainger College of Engineering,
University of Illinois Urbana-Champaign, Urbana, Illinois 61801, USA*

³*Illinois Center for Advanced Studies of the Universe and Department of Physics,
The Grainger College of Engineering, University of Illinois Urbana-Champaign, Urbana, Illinois 61801, USA*

⁴*Anthony J. Leggett Institute for Condensed Matter Theory, The Grainger College of Engineering,
University of Illinois Urbana-Champaign, Urbana, Illinois 61801, USA*

⁵*Department of Physics, The Ohio State University, Columbus, OH 43210, USA*

⁶*Department of Materials Science and Engineering, The Grainger College of Engineering,
University of Illinois Urbana-Champaign, Urbana, Illinois 61801, USA*

In a system of charged chiral fermions driven out of equilibrium, an electric current parallel to the magnetic field can generate a dynamic instability by which electromagnetic waves become amplified. Whether a similar instability can occur in chiral solid-state systems remains an open question. Using time-domain terahertz (THz) emission spectroscopy, we detect signatures of what we dub a “dynamic magneto-chiral instability” in elemental tellurium, a structurally chiral crystal. Upon transient photoexcitation in a moderate external magnetic field, tellurium emits THz radiation consisting of coherent modes that amplify over time. An explanation for this amplification is proposed using a theoretical model based on a dynamic instability of electromagnetic waves interacting with infrared-active oscillators of impurity acceptor states in tellurium to form an amplifying polariton. Our work not only uncovers the presence of a magneto-chiral instability but also highlights its promise for THz-wave amplification in chiral materials.

Magnetic fields can induce anomalous, parity-breaking phenomena in chiral plasmas, i.e., systems with an inequivalent number of left- and right-handed chiral particles. A well-known example of such phenomena is the chiral magnetic effect (CME), where the existence of a chiral anomaly generates an electric current \mathbf{j} parallel to an applied magnetic field \mathbf{B} , $\mathbf{j} = \sigma_M \mathbf{B}$ [1]. Here, σ_M is a pseudoscalar that is odd under inversion and even under time reversal, reflecting the symmetries of the current \mathbf{j} and the magnetic field \mathbf{B} . The CME is predicted in quark-gluon plasmas and can lead to a dynamic instability that amplifies magnetic fields as a function of time [2–4]. Such a chiral plasma instability has garnered

interest across various research fields such as early universe physics [5], supernovas [6], turbulence-driven dynamos in the post-merger phase of binary neutron star coalescence [7], and quark-gluon plasma studies [8]. In solid state systems, the CME is evidenced in transport measurements on Weyl semi-metals [9, 10], and the associated dynamic instability is predicted to manifest as an anomalous reflectance of light from the surface of a time-reversal-breaking Weyl semi-metal prepared in a non-equilibrium steady state [11].

Going beyond the CME in chiral plasmas, we propose that magneto-chiral currents $\mathbf{j} = \sigma_M \mathbf{B}$ in structurally chiral crystals driven out of equilibrium may also give rise to a dynamic instability. σ_M , which transforms like a pseudoscalar (or an electric toroidal monopole), is symmetry-allowed in chiral crystals [12]. Although in equilibrium σ_M must vanish according to band theory [13], a finite-frequency response is still possible [14]. Furthermore, if an excitation generates an out-of-equilibrium unequal occupation of left-handed and right-handed electronic states in a transient state that is sufficiently long-lived, a magneto-chiral current analogous to the CME can arise. Note that the imbalance between left-handed and right-handed electronic states can exist in chiral crystals even without the presence of emergent Weyl fermions at low energies. As we show in this work, in the presence of electromagnetic waves, the out-of-equilibrium crystal with nonzero σ_M can display a dynamic magneto-chiral instability manifested as an amplified response.

We use time-domain THz emission spectroscopy in a magnetic field to reveal signatures of the proposed magneto-chiral dynamic instability in elemental tellurium, a nonmagnetic structurally-chiral crystal. Tellurium features helical atomic chains along its chiral axis \mathbf{c} [see Fig. 1(a-b)], allowing nonreciprocal transport [15] and current-induced magnetization [16]. We photoexcite tellurium in an external magnetic field \mathbf{B}_0 using an ultrafast near-infrared (NIR) pulse with energy 1.2 eV (greater than the 0.32 eV band-gap of semicon-

* These authors contributed equally to this work.

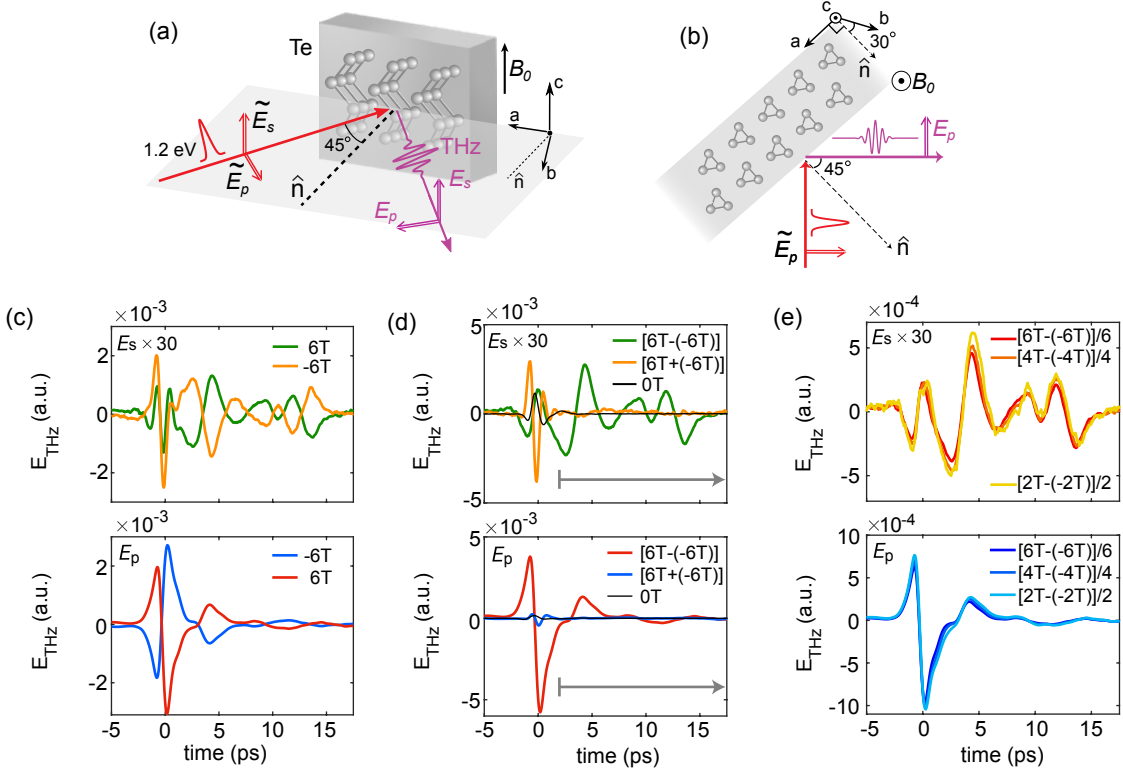


FIG. 1. **THz emission from tellurium in an external magnetic field.** **a(b)** The side (top) view of the sample geometry. The helical axis c is oriented parallel to the sample surface, which corresponds to the natural cleavage plane ($10\bar{1}0$) of tellurium. The near-infrared (NIR) pump is incident onto the sample surface at 45° . The THz emission is collected at 90° from the incident NIR pump and is detected as either E_s ($\parallel B_0$) or E_p ($\perp B_0$). The sample surface normal is denoted with a dashed arrow \hat{n} , the rotation around which allows access to $B_0 \parallel c$ (shown in **a**, **b**) and $B_0 \perp c$ sample orientations. **c** E_s and E_p for $B_0 = \pm 6$ T at a temperature of 17 K. **d** The B_0 -symmetrized and B_0 -antisymmetrized THz emission, along with the THz emission at 0 T. The gray arrows mark the time window in which the 0 T and B_0 -symmetrized emission data are almost negligible but the B_0 -antisymmetrized emission data still show coherent oscillations. **e** B_0 -antisymmetrized data re-scaled by dividing the magnetic field amplitude $|B_0|$.

ducting tellurium [17]). The photoexcitation generates a transient current and coherent modes that radiate THz waves, the electric field of which we resolve in the time domain using standard electro-optic sampling (Methods). We find that the radiated THz polarized along B_0 contains coherent modes that unexpectedly increase in amplitude over time, consistently across varying magnetic fields and temperatures. We conjecture that this amplification is a signature of a dynamic instability in photoexcited tellurium at frequencies well below the band gap and approaching the hydrodynamic limit for charge carriers. To justify this conjecture, we develop a theoretical model in which the magneto-chiral instability is manifested in the polariton consisting of THz light coupled with an IR-active oscillator associated with a tellurium impurity level to form a polariton, leading to an amplifying, radiative instability that explains the observed THz amplification.

Figure 1a,b show the side view and top view of the experimental geometry, respectively. The helical axis c of tellurium lies in the sample plane, and the NIR pulse

is incident at 45° to the sample normal \hat{n} . The emitted THz is collected at 90° away from the incident NIR. Fig. 1c shows the measured time profiles of the THz electric field ($E_{\text{THz}}(t)$) emitted from Te upon photoexcitation at a temperature of $T = 7$ K and an external magnetic field $B_0 \parallel c$ of ± 6 T. Here the incident NIR pump is either s -polarized (electric field component \tilde{E}_s along B_0) or p -polarized (electric field component \tilde{E}_p perpendicular to B_0). Note that experiments were performed for two sample orientations: $B_0 \parallel c$ (shown in Fig. 1) and $B_0 \perp c$. To study the response that is odd or even with respect to the external magnetic field, we show the B_0 -antisymmetrized THz emission [(+6 T) data subtracted by (-6 T) data] and the B_0 -symmetrized [sum of (+6 T) and (-6 T) data], together with the 0 T THz emission in Fig. 1d. The sharp signal at $t = 0$ ps lasting for about 1 ps observed in B_0 -symmetrized and the 0 T THz emission scan can be attributed to a photo-Dember effect from electron-hole mobility differences near the sample surface [18]. Strikingly, the B_0 -antisymmetrized data shows coherent oscillations that persist for a much longer time

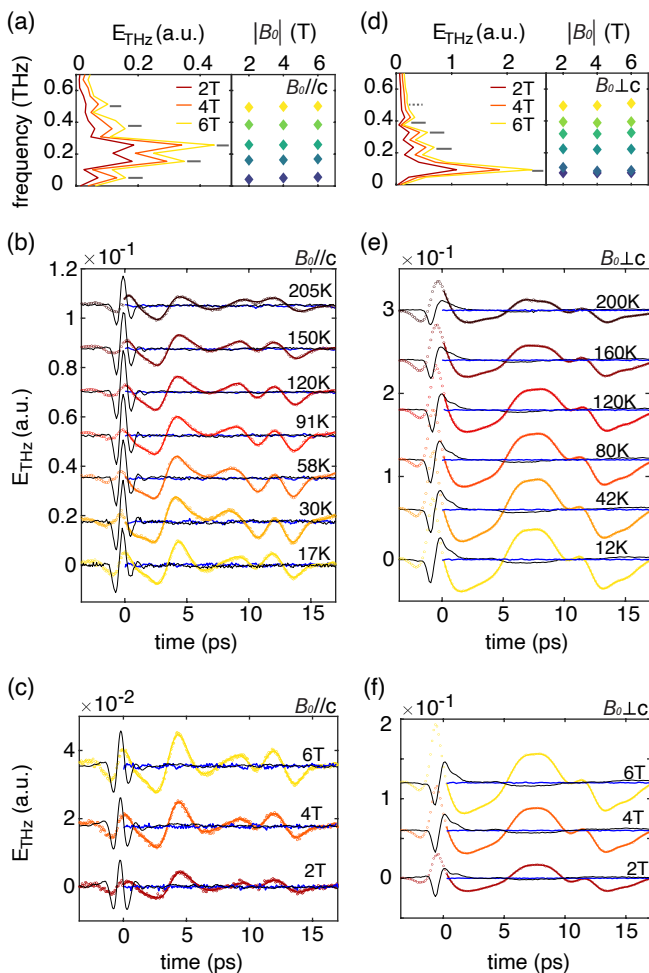


FIG. 2. **Temperature and field-dependence of the E_s polarized THz emission S_{odd} .** **a-c** Data for the $B_0 \parallel c$ sample orientation: **a** Fourier transform of the E_s emission S_{odd} , with the $|B_0|$ dependence of the extracted mode frequencies summarized in the right panel. Modes are color-coded based on their frequency values. **b** Fit to the temperature-dependent E_s emission S_{odd} at 6 T. Colored circles represent the data, colored lines are the time-domain fits, and blue traces show the residuals. Black lines represent the B_0 -symmetrized emissions, providing a reference for $t = 0$. **c** Fit to the $|B_0|$ -dependent E_s emission S_{odd} at 17 K. **d-f** Data for the $B_0 \perp c$ sample orientation: **d** Fourier transform of the E_s emission S_{odd} , and the $|B_0|$ dependence of the extracted mode frequencies. **e** Fit to the temperature-dependent E_s emission data at 6 T. **f** Fit to the $|B_0|$ -dependent E_s emission S_{odd} at 12 K. In **a** and **d** left panels, gray bars denote the linear-prediction-extracted mode frequencies averaged over different fields, with the one dashed bar indicating uncertainty due to the mode being near the noise level.

(shown for up to 17.5 ps in Fig. 1d) than typical THz emission due to just a photo-Dember effect. In contrast note that the 0 T and B_0 -symmetrized data show no THz emission after about 2 ps (time-window indicated by the gray arrow in Fig. 1d). The long-lasting signal in the B_0 -antisymmetrized data is also clearly evident in

the raw THz emission from s -polarized pump (top panel, Fig. 1c). We further note that the B_0 -antisymmetrized emission at all times scales nearly linearly with the applied external magnetic field B_0 : scaling the emitted B_0 -antisymmetrized time profiles with B_0 results in all curves nearly overlapping, as shown in Fig. 1e.

Possible reasons for the increase in THz emission with increasing B_0 include a radiating Hall current or rotation of a surface dipole radiation by an external magnetic field [19, 20]. These effects will enhance the THz emission *only* in the $E_p(\perp B_0)$ direction [19, 20], as the Lorentz force is always perpendicular to B_0 . For the remainder of the work, we thus focus on the $E_s(\parallel B_0)$ anti-symmetrized emission (referred to as S_{odd} in the remainder of the text), which is not affected by the transport Hall current.

Figure 2a shows the Fourier transform of S_{odd} for $B_0 \parallel c$. This frequency domain data consists of five main peaks, whose frequencies do not change significantly with magnetic field. Based on this observation, we apply a non-iterative time-domain linear prediction algorithm [21] to the time-domain THz data S_{odd} . Linear prediction decomposes the data into a sum of harmonic oscillators with exponential factors $\sum_i A_i e^{\beta_i t} \cos(\omega_i t + \phi_i)$. This procedure requires no initial fit parameters and uniquely fits noise-free sinusoidal data with exponential envelopes (SI Sec.A), whereas for noisy data, it reliably identifies sinusoidal components above the noise level, as shown in NMR [22] and pump-probe spectroscopy [23]. We find that constraining the fitting algorithm for S_{odd} to allow only decaying exponentials ($\beta < 0$) does not fit the data well - there are significant residuals with amplitudes increasing with time (SI Fig. S1). In contrast, allowing for growing exponentials ($\beta > 0$) accurately describes both the magnetic field and temperature dependent S_{odd} data as shown in Fig. 2b-c. The time-domain linear prediction fits (colored solid lines) closely match the data (empty circles), with negligible residuals (blue solid lines). We performed the same analysis for the S_{odd} signal measured for $B_0 \perp c$, and find that allowing $\beta > 0$ is necessary for obtaining fits that accurately describe the data, as shown in Fig. 2e-f. From the fitting, we extract five distinct sinusoidal modes for both sample orientations. The extracted frequencies of these modes are shown in the right panels of Fig. 2a and Fig. 2d. As expected from the scaling behavior of the time-domain data (Fig. 1e), there is negligible dependence of the mode frequencies on the external magnetic field. We further note two caveats to the extracted modes shown in Fig. 2d: the small splitting of the < 0.1 THz mode is attributed to mode chirp (SI Sec. A); and the amplitude of the highest-frequency mode is close to the noise level. These caveats do not affect the main conclusions of this work.

Having developed a reliable method to extract the dynamics of the modes contributing to S_{odd} , we next determine their possible origin. Since these modes radiate in the far-field, they must have a net infrared-dipole moment and, given that the crystal structure of tellurium

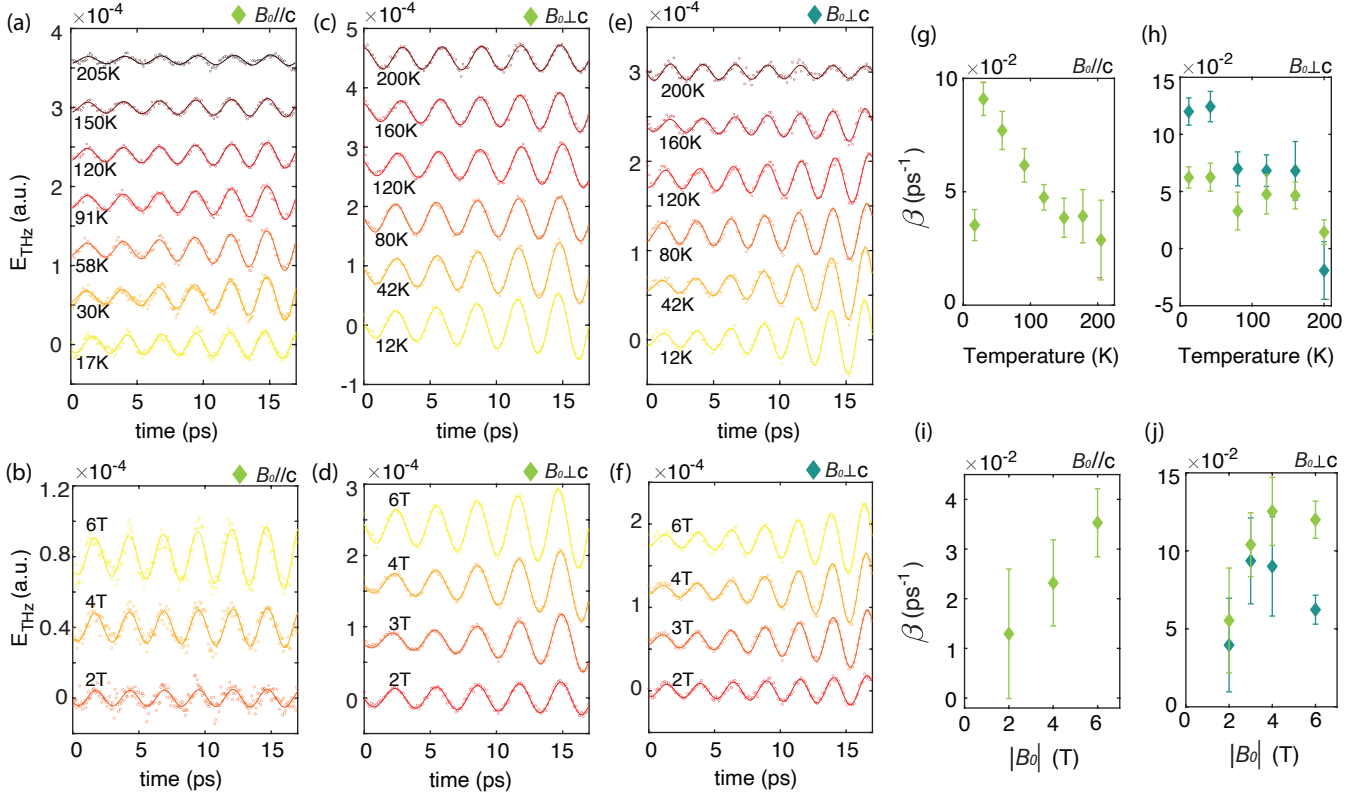


FIG. 3. **The amplified modes in the E_s THz emission S_{odd} .** **a-b** E_s -polarized S_{odd} , with $\mathbf{B}_0 \parallel \mathbf{c}$. **a** Temperature dependence of the 0.37 THz mode at 6 T. **b** Same as **a**, but showing the $|\mathbf{B}_0|$ dependence at 17 K. **c-f** E_s -polarized S_{odd} with $\mathbf{B}_0 \perp \mathbf{c}$. **c** Temperature dependence of the 0.32 THz mode at 6 T. **d** Same as **c**, but showing $|\mathbf{B}_0|$ dependence at 12 K. **e** Temperature dependence of the 0.39 THz mode for S_{odd} taken at 6 T. **f** Same as **e**, but showing $|\mathbf{B}_0|$ dependence at 12 K. In **a-f**, colored circles represent the data after subtracting time-domain fit components of all other modes, and colored lines show the fits for the modes using parameters obtained from the linear prediction model. **g, h** Temperature dependence of the amplification rate β for $\mathbf{B}_0 \parallel \mathbf{c}$ and $\mathbf{B}_0 \perp \mathbf{c}$, respectively. Color-coding of the modes for a given sample orientation is consistent with symbols on the upper right of **a-f** and with the color-coding in Fig. 2 **a** and **d**. For $\mathbf{B}_0 \perp \mathbf{c}$, 0.32 THz (0.39 THz) is denoted with dark green (light green) symbols. **i, j** $|\mathbf{B}_0|$ dependence of the amplification rate β for $\mathbf{B}_0 \parallel \mathbf{c}$ and $\mathbf{B}_0 \perp \mathbf{c}$, respectively. The error bars in panels **g-j** are obtained from an additional least square fit using the output of the linear prediction model as initial parameters.

breaks inversion symmetry, suggesting the modes may originate from optical phonons. However, the frequencies of the observed modes are much smaller than any of tellurium's optical phonons [18, 24]. Moreover, the absence of coherent oscillations in a 1030 nm pump - 515 nm transient reflectivity probe measurement under $\mathbf{B}_0 \parallel \mathbf{c}$ (SI Sec. B) indicates that they are not Raman-active. Instead, the energies of the observed modes are close to the energies of acceptor states in tellurium due to impurities (e.g. selenium or group V elements) [25–28] as measured previously in infrared magneto-transmission experiments. Those results also showed negligible \mathbf{B}_0 -field dependence of the energies [25, 29, 30], consistent with our observations (SI Sec. C). The mode frequencies differ between the two sample orientations (gray bars in Fig. 2b-c), likely due to the anisotropic nature of tellurium.

We next focus on the modes in S_{odd} that are described

by exponentially growing sinusoids ($\beta > 0$) and investigate their temperature and field dependence. We isolate the $\beta > 0$ modes by subtracting the time-domain fits of all the other modes. In the $\mathbf{B}_0 \parallel \mathbf{c}$ measurement geometry, Fig. 3a-b show the results for the 0.37 THz $\beta > 0$ mode. In the $\mathbf{B}_0 \perp \mathbf{c}$ geometry, Fig. 3c-d show the results for the 0.32 THz $\beta > 0$ mode and Fig. 3e-f for the 0.39 THz $\beta > 0$ mode. The isolated mode trajectories (empty circles) overlap relatively well with the subtracted trajectories (solid lines). The dependence of β on the applied field and temperature is summarized in Fig. 3g-j, which shows that $\beta > 0$ consistently for these modes except at high temperature.

We now provide an interpretation of the amplifying components in the S_{odd} emissions by developing a model based on magneto-chiral currents. In general, the free-electron current density \mathbf{j} can be written as follows, assuming linear response on the Fourier domain of time and

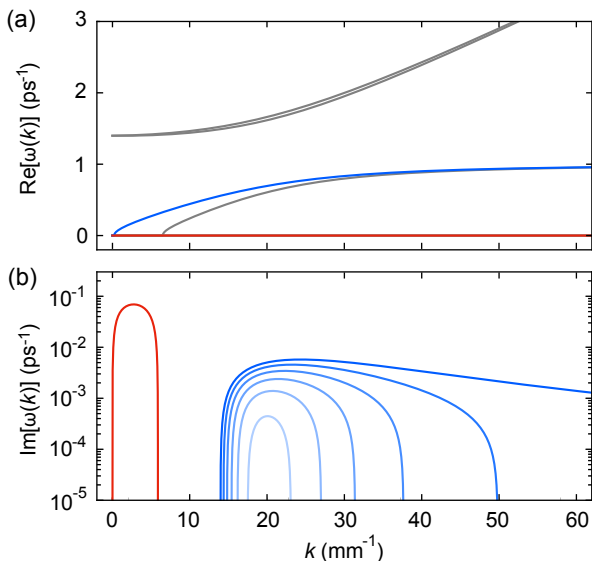


FIG. 4. **Calculated dispersions of the polariton illustrating the magneto-chiral dynamic instability.** **a** The $\text{Re}[\omega(k)]$ of the plane-wave solutions. Gray: Stable modes ($\text{Im}[\omega(k)] < 0$) with an avoided crossing, similar to the conventional polariton resulting from an IR-oscillator coupling with a photon. Red: A non-propagating ($\text{Re}[\omega(k)] = 0$) instability of the electromagnetic wave. Blue: The amplifying polariton with $\text{Re}[\omega(k)]$ pinned to ω_0 , assuming $\gamma = 0$. The $\text{Re}[\omega(k)]$ dispersions are mostly independent of γ . **b** The $\text{Im}[\omega(k)]$ of the solutions. Red: $\text{Im}[\omega(k)]$ of the non-radiating instability. Blue: $\text{Im}[\omega(k)]$ of the amplifying polariton assuming different γ . From dark blue to light blue, γ increases from 0 to $2.5 \times 10^{-2} \text{ ps}^{-1}$ in increments of $5 \times 10^{-3} \text{ ps}^{-1}$.

space:

$$\mathbf{j}(\omega, \mathbf{k}) = \sigma_M(\omega) \mathbf{B}(\omega, \mathbf{k}) + \sigma_E(\omega) \mathbf{E}(\omega, \mathbf{k}) \quad (1)$$

where \mathbf{E} and \mathbf{B} refer to the total electric and magnetic fields, respectively, as a function of the angular frequency ω and wave-vector \mathbf{k} , and σ_E is the electric conductivity. The pseudoscalar σ_M describes the frequency-dependent magneto-chiral conductivity. Importantly, $\sigma_M(\omega \rightarrow 0)$ vanishes in a near-equilibrium situation but can be nonzero for a non-equilibrium carrier distribution between electronic states with opposite chirality [14]. Thus, in the $\mathbf{k} \rightarrow 0$ limit, we assume that $\sigma_M(\omega)$ for a crystal driven out of equilibrium includes both adiabatic and frequency-dependent responses,

$$\sigma_M(\omega) = \frac{e^2}{4\pi^2 \hbar^2} \left[\mu_{\text{DC}} + \mu_{\text{AC}} \frac{\omega \tau}{\omega \tau + i} \right], \quad (2)$$

where μ_{AC} and μ_{DC} are real-valued parameters with dimensions of energy. This form satisfies causality in linear response. The frequency dependence of the μ_{AC} term can be derived from the Boltzmann equation in the single relaxation-time approximation [14], for which τ denotes the elastic scattering lifetime of free carriers. We emphasize that small perturbations near equilibrium do not

give rise to a finite μ_{DC} , which instead represents a far-from-equilibrium effect. By assuming constant μ_{DC} and μ_{AC} , we implicitly consider the system to be in a long-lived non-equilibrium transient state. This assumption is justified since, in our experiment, photoexcitation of tellurium causes a long-lived non-equilibrium carrier distribution in tellurium's conduction and valence bands, persisting over the time window shown in Figs. 1-3. Note that beyond this time-window ($> 30 \text{ ps}$), the THz emission data indicates that σ_M decays (i.e., μ_{AC} and μ_{DC} decay) between 20-30 ps (SI Sec. D), consistent with the carrier recombination time [31].

Given that the energies of the observed modes correspond to energies of impurity acceptor states, we model σ_E as a sum of the DC conductivity σ_{E0} and a contribution from the bound current,

$$\sigma_E(\omega) = \sigma_{E0} - \frac{i\omega C}{\omega_0^2 - \omega^2 - i\gamma\omega}. \quad (3)$$

The second term is the response of an infrared (IR)-active oscillator with intrinsic angular frequency ω_0 , damping rate γ , and $C = ne^2/m$ where n is the impurity concentration and m the oscillator mass [32].

Inserting Eqs. (1-3) into Maxwell's equations and using a plane-wave ansatz for electromagnetic fluctuations, $\mathbf{E}, \mathbf{B} \propto e^{i(\mathbf{k} \cdot \mathbf{r} - \omega t)}$, we calculate the dispersion relations $\omega(\mathbf{k})$ numerically. We use physically reasonable parameters: $\sigma_{E0} = 50 \text{ } \Omega^{-1} \text{ m}^{-1}$ [33], $\omega_0 = 1 \text{ ps}^{-1}$ (on the order of the observed mode frequencies), $n = 10^{16} \text{ cm}^{-3}$, $\mu_{\text{DC}} = 0.5 \text{ eV}$, $\mu_{\text{AC}} = -0.5 \text{ eV}$, $\tau = 1 \text{ ps}$, and the relative permittivity $\epsilon_r = 30$. Note that μ_{AC} and μ_{DC} approximate the energy difference between the pump laser photon (1.2 eV) and tellurium's band gap (0.32 eV). The results are shown in Fig. 4a for the real part $\text{Re}[\omega(k)]$ and in Fig. 4b for the imaginary part $\text{Im}[\omega(k)]$, with both depending only on $k = |\mathbf{k}|$ due to the model isotropy. Two unstable solutions ($\text{Im}[\omega(k)] > 0$, red and blue) are present, implying that these electromagnetic modes grow as $e^{\text{Im}[\omega(k)]t}$. We associate these modes to the magneto-chiral dynamical instability. The stable modes ($\text{Im}[\omega(k)] < 0$, gray lines in Fig. 4a) are the conventional damped polariton arising due to the coupling between the IR-active mode and the electromagnetic wave [34]. The slight degeneracy lift is due to helicity-breaking σ_M . One of the two instabilities shown in Fig. 4 (red) is non-radiative with vanishing group velocity and Poynting vector. This instability resembles the chiral plasma instability discussed in Ref. [2] and occurs due to $\mu_{\text{DC}} \neq 0$. Adding a Hall current under an external magnetic field enables propagation of this red instability, reproducing the chiral magnetic instability noted in Refs. [11, 35]. However, an unrealistically large value of μ_{DC} would be required to observe this red instability in the THz frequency range of the oscillators in S_{odd} (SI Sec. E).

In contrast, the second magneto-chiral instability (blue in Fig. 4) is radiative ($\text{Re}[\omega(k)] \neq 0$) for the physically reasonable parameters noted above. Moreover, the angular frequency is pinned at $\text{Re}[\omega(k)] \approx \omega_0 = 1 \text{ ps}^{-1}$ for

k larger than 25 mm^{-1} , which is the value that maximizes $\text{Im}[\omega(k)]$. This frequency pinning arises from the polaritonic coupling, where the IR-active oscillator gains instability through its interaction with the electron fluid via electromagnetic waves. Such polaritonic coupling via the magneto-chiral instability can be generalized to other IR-active oscillators (e.g. optical phonons). We note that the generation of collective modes with large wave vectors up to $k \sim 100 \text{ mm}^{-1}$ is allowed given the short laser penetration depth (300 nm [36], considerably shorter than the emitted THz wavelength). While we do not track the time evolution of μ_{DC} and μ_{AC} in the model, it is reasonable to expect that the energy to power the radiative instability due to a finite μ_{AC} is supplied by the decay of the non-zero μ_{DC} , which represents the system relaxing from a far-out-of-equilibrium state.

As shown in Fig. 4b, without damping ($\gamma = 0$), the radiative instability's $\text{Im}[\omega(k)]$ of approximately 10^{-2} ps^{-1} aligns within an order of magnitude with the observed β . As γ increases, the amplification rate $\text{Im}[\omega(k)]$ of the instability decreases. γ is sensitive to disorder, phonon scattering, and local potentials in cyclotron motions, and it typically increases with temperature and decreases with magnetic field under lower fields [37]. Thus, we expect the amplification rate to decrease (increase) with temperature (magnetic field at lower fields), which is indeed observed in the experimentally extracted β , see Fig. 3g-j. Note that if γ exceeds $3 \times 10^{-2} \text{ ps}^{-1}$, then the radiative instability vanishes ($\text{Im}[\omega(k)]$ is no longer > 0), which provides a viable explanation for the experimental observation that only a subset of the IR-active modes are amplified over time (those with smaller γ).

We next discuss the crystal symmetry requirements for generating a magneto-chiral current with photoexcitation. In a crystal, the coefficient σ_{M} is replaced by a rank-2 tensor $\sigma_{\text{M},ij}$ that relates the current component j_i with the magnetic field component B_j , as discussed in Ref [14]. The non-zero elements of this tensor for a given crystal structure can be derived via group theory. Using the facts that Te has the chiral space group $P3_121$ with corresponding point group D_3 , and that the out-of-plane (in-plane) components of both the current and the magnetic field transform as the same non-trivial irreducible representation $A_2 (E)$ of D_3 , it follows that $\sigma_{\text{M},ij}$ is a diagonal tensor with $\sigma_{\text{M},xx} = \sigma_{\text{M},yy} \neq \sigma_{\text{M},zz}$ [38]. This reflects the fact that a pseudoscalar transforms as the trivial irreducible representation, as expected for any of the 11 enantiomorphic point groups [39]. However, symmetry alone is insufficient to ensure a finite current, since μ_{DC} is only non-zero in a far-from-equilibrium situation where electronic states with opposite chirality have different occupations. In our experiment, we expect that after the initial photoexcitation, charge fluctuations that preserve the crystalline symmetries (i.e., that transform as the A_1 irreducible representation) will be the long lived ones [40, 41]. Since the pseudoscalar also transforms as the A_1 irreducible representation, the photoexcitation can potentially generate a long-lived non-equilibrium dis-

tribution of carriers with a net chirality.

We note that the microscopic origin of μ_{DC} and μ_{AC} depends on the properties of the underlying band structure, as discussed in [14]. While chiral-imbalanced Weyl nodes in tellurium have been previously reported to lead to a CME [10], which can be described with a μ_{DC} term, the Weyl nodes are located a few hundreds of meV away from the middle of the band gap [10, 42–45]. Future studies of the non-equilibrium carrier distributions (e.g., using time-resolved ARPES experiments combined with DFT calculations) can provide further insights into the microscopic origin of the magneto-chiral dynamic instability in tellurium. Importantly, we emphasize that our analysis relies only on the chiral symmetry of the crystal structure of tellurium, and not on the precise microscopic mechanisms at play. Our findings highlight the potential to manipulate THz-range electromagnetic waves in far-out-of-equilibrium chiral materials, including wave amplification.

Acknowledgments: We thank Enrico Speranza, Rong Zhang, Yingkai Liu, Taylor Hughes, and Thomas P. Devereux for useful discussions. This work was supported by the Quantum Sensing and Quantum Materials, an Energy Frontier Research Center funded by the U.S. Department of Energy (DOE), Office of Science, Basic Energy Sciences (BES), under Award No. DE-SC0021238 (project conception, data acquisition and analysis, and manuscript preparation). F.M., Y.L., A.M., and C.L. acknowledge support from NSF Career Award No. DMR-2144256 for the development of the experimental setup. F.M. acknowledges support from the EPiQS program of the Gordon and Betty Moore Foundation, Grant GBMF11069. Y.H. acknowledges support from the IQUIST (Illinois Quantum Information Science and Technology Center) Postdoctoral Fellowship. P.Z. was supported by the Center for Emergent Materials, an NSF MRSEC, under award number DMR-2011876. R.M.F. (theoretical model) was supported by the Air Force Office of Scientific Research under Award No. FA9550-21-1-0423.

Author contributions: Y.H. performed sample characterization, the THz emission experiments, and the corresponding data analysis. Y.L., A.M., Y.H., C.L., and F.M. designed and built the THz emission setup compatible with a magnetic field. D.P. and J.Y.Y. assisted with the THz emission measurements without the echo. N.A., Y.H., P.Z., R.M.F., and J.N. developed the theoretical understanding and modeling of the magneto-chiral instability. E.A.P. performed preliminary synthesis reactions and assisted Y.H. with structural characterization, supervised by D.P.S. D.C. and P.A. provided insights into the impurity levels in tellurium. Y.H., N.A., P.Z., R.M.F., J.N., and F.M. wrote the manuscript with input from all the authors. F.M. conceived and supervised this project.

Competing interests: The authors declare no competing interests.

Methods: THz emission measurements were performed with our custom-built time-domain THz spectroscopy setup based on a Yb:KGW amplifier laser (PHAROS, Light Conversion). The fundamental laser pulse wavelength is 1030 nm with a pulse duration of ~ 160 fs. The fundamental beam is split into a pump and a probe, with the pump incident onto the sample at a 45° angle-of-incidence while the probe is used for electro-optic sampling (EOS) of the emitted THz field. The sample is mounted at the center of a magneto-optic cryostat (OptiCool, Quantum Design) with TPX windows to allow THz transmission. The THz field radiated by the sample is collected and collimated at 90° from the pump beam and at a 45° angle relative to the sample normal, using a THz-transmissive TPX lens mounted inside the cryostat. The emitted THz is then focused onto a (110)-cut CdTe crystal. The EOS probe beam is made to spatially and temporally overlap with the emitted THz on the CdTe crystal. The THz field $\mathbf{E}(t)$ is thus measured by scan-

ning the time delay of the 1030 nm electro-optic sampling beam relative to the emitted THz field [46]. The detection bandwidth of the CdTe crystal decreases above 1 THz [47]. The experiments were performed with two prototypical sample orientations, $\mathbf{B}_0 \parallel \mathbf{c}$ and $\mathbf{B}_0 \perp \mathbf{c}$, which can be accessed by rotating the sample. To selectively detect the THz emission component \mathbf{E}_s parallel to the \mathbf{B} field or the component \mathbf{E}_p perpendicular to the \mathbf{B} field, we rotated four optical components: the THz wire grid polarizer (WGP) with an extinction ratio 10^{-3} , the half-wave plate, and polarizer for the 1030 nm probe, and the CdTe crystal for EO sampling. The WGP has an extinction ratio of better than 10^{-3} .

Data availability: The data in this manuscript is available at Illinois Data Bank [48].

Corresponding authors: Correspondence to Yijing Huang (huangyj@illinois.edu) and/or Fahad Mahmood (fahad@illinois.edu).

-
- [1] K. Fukushima, D. E. Kharzeev, and H. J. Warringa, Chiral magnetic effect, *Phys. Rev. D* **78**, 074033 (2008).
- [2] Y. Akamatsu and N. Yamamoto, Chiral plasma instabilities, *Phys. Rev. Lett.* **111**, 052002 (2013).
- [3] Y. Akamatsu and N. Yamamoto, Chiral langevin theory for non-abelian plasmas, *Phys. Rev. D* **90**, 125031 (2014).
- [4] I. A. Shovkovy, Anomalous plasma: chiral magnetic effect and all that, in *Peter Suranyi 87th Birthday Festschrift A Life in Quantum Field Theory* (World Scientific, 2023) pp. 291–316.
- [5] A. Boyarsky, J. Fröhlich, and O. Ruchayskiy, Self-consistent evolution of magnetic fields and chiral asymmetry in the early universe, *Phys. Rev. Lett.* **108**, 031301 (2012).
- [6] N. Yamamoto, Chiral transport of neutrinos in supernovae: Neutrino-induced fluid helicity and helical plasma instability, *Phys. Rev. D* **93**, 065017 (2016).
- [7] E. R. Most, Impact of a mean field dynamo on neutron star mergers leading to magnetar remnants, *Phys. Rev. D* **108**, 123012 (2023), arXiv:2311.03333 [astro-ph.HE].
- [8] Y. Hirono, D. E. Kharzeev, and Y. Yin, Self-similar inverse cascade of magnetic helicity driven by the chiral anomaly, *Phys. Rev. D* **92**, 125031 (2015).
- [9] J. Xiong, S. K. Kushwaha, T. Liang, J. W. Krizan, M. Hirschberger, W. Wang, R. J. Cava, and N. P. Ong, Evidence for the chiral anomaly in the dirac semimetal Na_3Bi , *Science* **350**, 413 (2015).
- [10] N. Zhang, G. Zhao, L. Li, P. Wang, L. Xie, B. Cheng, H. Li, Z. Lin, C. Xi, J. Ke, *et al.*, Magnetotransport signatures of weyl physics and discrete scale invariance in the elemental semiconductor tellurium, *Proceedings of the National Academy of Sciences* **117**, 11337 (2020).
- [11] Y. Nishida, Chiral light amplifier with pumped weyl semimetals, *Phys. Rev. Lett.* **130**, 096903 (2023).
- [12] H. Kusunose, J.-i. Kishine, and H. M. Yamamoto, Emergence of chirality from electron spins, physical fields, and material-field composites, *Applied Physics Letters* **124**, 260501 (2024).
- [13] Y. Chen, S. Wu, and A. A. Burkov, Axion response in weyl semimetals, *Phys. Rev. B* **88**, 125105 (2013).
- [14] S. Zhong, J. E. Moore, and I. Souza, Gyrotropic magnetic effect and the magnetic moment on the fermi surface, *Phys. Rev. Lett.* **116**, 077201 (2016).
- [15] F. Calavalle, M. Suárez-Rodríguez, B. Martín-García, A. Johansson, D. C. Vaz, H. Yang, I. V. Maznichenko, S. Ostanin, A. Mateo-Alonso, A. Chuvilin, I. Mertig, M. Gobbi, F. Casanova, and L. E. Hueso, Gate-tuneable and chirality-dependent charge-to-spin conversion in tellurium nanowires, *Nature Materials* **21**, 526 (2022).
- [16] T. Furukawa, Y. Shimokawa, K. Kobayashi, and T. Itou, Observation of current-induced bulk magnetization in elemental tellurium, *Nature Communications* **8**, 954 (2017).
- [17] R. S. Caldwell and H. Y. Fan, Optical properties of tellurium and selenium, *Phys. Rev.* **114**, 664 (1959).
- [18] T. Dekorsy, H. Auer, H. J. Bakker, H. G. Roskos, and H. Kurz, Thz electromagnetic emission by coherent infrared-active phonons, *Phys. Rev. B* **53**, 4005 (1996).
- [19] M. B. Johnston, D. M. Whittaker, A. Corchia, A. G. Davies, and E. H. Linfield, Simulation of terahertz generation at semiconductor surfaces, *Phys. Rev. B* **65**, 165301 (2002).
- [20] J. Shan, C. Weiss, R. Wallenstein, R. Beigang, and T. Heinz, Origin of magnetic field enhancement in the generation of terahertz radiation from semiconductor surfaces, *Optics Letters* **26**, 849 (2001).
- [21] H. Barkhuijsen, R. de Beer, W. Bovée, and D. van Ormondt, Retrieval of frequencies, amplitudes, damping factors, and phases from time-domain signals using a linear least-squares procedure, *Journal of Magnetic Resonance* (1969) **61**, 465 (1985).
- [22] J. J. Led and H. Gesmar, Application of the linear prediction method to NMR spectroscopy, *Chemical Reviewsews* **91**, 1413 (1991).
- [23] Y. Huang, S. Teitelbaum, S. Yang, G. De la Peña, T. Sato, M. Chollet, D. Zhu, J. L. Niedziela, D. Bansal, A. F. May, A. M. Lindenberg, O. Delaire, M. Trigo, and D. A. Reis, Nonthermal bonding origin of a novel pho-

- toexcited lattice instability in sncs, Phys. Rev. Lett. **131**, 156902 (2023).
- [24] B. Torrie, Raman spectrum of tellurium, Solid State Communications **8**, 1899 (1970).
- [25] Y. Couder, M. Hulin, and H. Thomé, Cyclotron resonance in tellurium, Phys. Rev. B **7**, 4373 (1973).
- [26] O. Betbeder-Matibet and M. Hulin, A Semi-Empirical Model for the Valence Band Structure of Tellurium, Physica Status Solidi (B) **36**, 573 (1969).
- [27] T. Tani and S. Tanaka, Pressure effect on the impurity state and impurity conduction in tellurium, in *The Physics of Selenium and Tellurium: Proceedings of the International Conference on the Physics of Selenium and Tellurium, Königstein, Fed. Rep. of Germany, May 28–31, 1979* (Springer, 1979) pp. 142–152.
- [28] K. Natori, T. Ando, M. Tsukada, K. Nakao, and Y. Uemura, The acceptor states in tellurium, Journal of the Physical Society of Japan **34**, 1263 (1973).
- [29] D. Hardy, C. Rigaux, J. P. Vieren, and N. H. Hau, Impurities and intervalence band magneto-optical transitions in tellurium, Physica Status Solidi (B) **47**, 643 (1971).
- [30] H. Shinno, R. Yoshizaki, S. Tanaka, T. Doi, and H. Kamimura, Conduction band structure of tellurium, Journal of the Physical Society of Japan **35**, 525 (1973).
- [31] G. Jnawali, Y. Xiang, S. M. Linser, I. A. Shojaei, R. Wang, G. Qiu, C. Lian, B. M. Wong, W. Wu, P. D. Ye, *et al.*, Ultrafast photoinduced band splitting and carrier dynamics in chiral tellurium nanosheets, Nature Communications **11**, 3991 (2020).
- [32] M. Dressel and G. Grüner, *Electrodynamics of Solids: Optical Properties of Electrons in Matter* (Cambridge University Press, Cambridge ; New York, 2002).
- [33] V. E. Bottom, The hall effect and electrical resistivity of tellurium, Science **115**, 570 (1952).
- [34] K. Huang, On the interaction between the radiation field and ionic crystals, Proceedings of the Royal Society of London. Series A. Mathematical and Physical Sciences **208**, 352 (1951).
- [35] T. Amitani and Y. Nishida, Dynamical chiral magnetic current and instability in weyl semimetals, Phys. Rev. B **107**, 014302 (2023).
- [36] S. Tutihasi, G. Roberts, R. Keezer, and R. Drews, Optical properties of tellurium in the fundamental absorption region, Physical Review **177**, 1143 (1969).
- [37] M. Hopkins, R. Nicholas, D. Barnes, M. Brummell, J. Harris, and C. Foxon, Temperature dependence of the cyclotron-resonance linewidth in GaAs-Ga_{1-x}Al_xAs heterojunctions, Physical Review B **39**, 13302 (1989).
- [38] W.-Y. He and K. T. Law, Magnetoelectric effects in gyrotropic superconductors, Phys. Rev. Res. **2**, 012073 (2020).
- [39] E. M. Anastassakis, Morphic effects in lattice dynamics, in *Dynamical properties of solids*, Vol. 4 (Elsevier, 1980) p. 357.
- [40] J. J. Li, J. Chen, D. A. Reis, S. Fahy, and R. Merlin, Optical probing of ultrafast electronic decay in Bi and Sb with slow phonons, Phys. Rev. Lett. **110**, 047401 (2013).
- [41] S. M. O'Mahony, F. Murphy-Armando, E. D. Murray, J. D. Querales-Flores, I. Savić, and S. Fahy, Ultrafast relaxation of symmetry-breaking photo-induced atomic forces, Phys. Rev. Lett. **123**, 087401 (2019).
- [42] G. Chang, B. J. Wieder, F. Schindler, D. S. Sanchez, I. Belopolski, S.-M. Huang, B. Singh, D. Wu, T.-R. Chang, T. Neupert, *et al.*, Topological quantum properties of chiral crystals, Nature materials **17**, 978 (2018).
- [43] J. Ma, B. Cheng, L. Li, Z. Fan, H. Mu, J. Lai, X. Song, D. Yang, J. Cheng, Z. Wang, C. Zeng, and D. Sun, Unveiling weyl-related optical responses in semiconducting tellurium by mid-infrared circular photogalvanic effect, Nature Communications **13**, 5425 (2022).
- [44] J. Chen, T. Zhang, J. Wang, L. Xu, Z. Lin, J. Liu, C. Wang, N. Zhang, S. P. Lau, W. Zhang, *et al.*, Topological phase change transistors based on tellurium weyl semiconductor, Science advances **8**, eabn3837 (2022).
- [45] M. Hirayama, R. Okugawa, S. Ishibashi, S. Murakami, and T. Miyake, Weyl node and spin texture in trigonal tellurium and selenium, Phys. Rev. Lett. **114**, 206401 (2015).
- [46] P. C. Planken, H.-K. Nienhuys, H. J. Bakker, and T. Wenckebach, Measurement and calculation of the orientation dependence of terahertz pulse detection in ZnTe, JOSA B **18**, 313 (2001).
- [47] X. Ropagnol, M. Matoba, J. E. Nkeck, F. Blanchard, E. Isgandarov, J. Yumoto, and T. Ozaki, Efficient terahertz generation and detection in cadmium telluride using ultrafast ytterbium laser, Applied Physics Letters **117**, 181101 (2020).
- [48] Y. Huang and M. Fahad, Observation of a magneto-chiral instability in photoexcited tellurium (2025), available from https://doi.org/10.13012/B2IDB-1409842_V1.